RESEARCH ARTICLE

Key Points:
- Globally the most important natural process changing interior ocean pH is organic matter remineralization
- $CaCO_3$ cycling has the largest impact on interior ocean pH in the northern Pacific and Indian Oceans
- Remineralization enhance anthropogenic pH change and while today this enhancement is small it may grow more important as ocean acidification continues

Supporting Information:
- Supporting Information S1

Correspondence to:
S. K. Lauvset,
siv.lauvset@norceresearch.no

Processes Driving Global Interior Ocean pH Distribution

S. K. Lauvset[1,2], B. R. Carter[3,4], F. F. Pèrez[5], L.-Q. Jiang[6,7], R. A. Feely[4], A. Velo[5], and A. Olsen[8]

[1]NORCE Norwegian Research Centre, Bjerknes Centre for Climate Research, Bergen, Norway, [2]Formerly at Geophysical Institute, University of Bergen, Bergen, Norway, [3]Joint Institute for the Study of the Atmosphere and Ocean, University of Washington, Seattle, WA, USA, [4]Pacific Marine Environmental Laboratory, National Oceanic and Atmospheric Administration, Seattle, WA, USA, [5]Instituto de Investigaciones Marinas, CSIC, Vigo, Spain, [6]Earth System Science Interdisciplinary Center, University of Maryland, College Park, MD, USA, [7]National Centers for Environmental Information, National Oceanographic and Atmospheric Administration, Silver Spring, MD, USA, [8]Geophysical Institute, University of Bergen and Bjerknes Centre for Climate Research, Bergen, Norway

Abstract Ocean acidification evolves on the background of a natural ocean pH gradient that is the result of the interplay between ocean mixing, biological production and remineralization, calcium carbonate cycling, and temperature and pressure changes across the water column. While previous studies have analyzed these processes and their impacts on ocean carbonate chemistry, none have attempted to quantify their impacts on interior ocean pH globally. Here we evaluate how anthropogenic changes and natural processes collectively act on ocean pH, and how these processes set the vulnerability of regions to future changes in ocean acidification. We use the mapped data product from the Global Ocean Data Analysis Project version 2, a novel method to estimate preformed total alkalinity based on a combination of a total matrix intercomparison and locally interpolated regressions, and a comprehensive uncertainty analysis. We find that the largest contribution to the interior ocean pH gradient comes from organic matter remineralization, with $CaCO_3$ cycling being the second most important process. The estimates of the impact of anthropogenic CO_2 changes on pH reaffirm the large and well-understood anthropogenic impact on pH in the surface ocean, and put it in the context of the natural pH gradient in the interior ocean. We also show that in the depth layer 500–1,500 m natural processes enhance ocean acidification by on average $28 \pm 15\%$, but with large regional gradients.

1. Introduction

Ocean pH is decreasing as a direct consequence of ocean uptake of carbon dioxide (CO_2) emitted during the burning of fossil fuels, cement production, and land use changes. This is commonly referred to as ocean acidification (Caldeira & Wickett, 2003; Feely et al., 2004, 2009). The decrease is well documented globally (e.g., Bates et al., 2014; Lauvset et al., 2015) and there is active research focused on understanding its consequences (e.g., Gattuso et al., 2015; Kroeker et al., 2013). The impacts of ocean acidification on marine life have proven to be complex, and there is now ample evidence that other factors such as food availability, predator-prey dynamics, and temperature changes affect an organism's response to ocean acidification (e.g., Kroeker et al., 2013). In a recent metaanalysis, Hurd and Cornwall (2015) highlighted the importance of considering natural gradients in carbonate chemistry for experimental design, in addition to ocean acidification-related chemistry changes.

Understanding the natural processes that determine ocean pH is also important when communicating ocean acidification research. Ocean acidification happens on top of several natural processes, and the combination of the two make some regions particularly vulnerable. One such region is the Southern Ocean, where upwelling of waters rich in remineralized carbon create a local minimum in carbonate ion concentrations in the thermocline. As shown by Negrete-García et al. (2019) this natural gradient means that a very small anthropogenic perturbation is sufficient to shift the aragonite saturation horizon by several hundred meters from one year to the next. A similar effect has been shown by Hauri et al. (2013), Feely et al. (2018), and Franco et al. (2018) for Eastern Boundary Upwelling Systems, which are also regions where natural processes act to enhance the impact of ocean acidification. Such research highlights the fact that ocean acidification decreases natural pH distributions that result from ocean mixing, biological production and remineralization, mineral dissolution, temperature changes, and gas exchange.

Several studies have addressed how natural processes determine the ocean mean distribution of pH (e.g., Feely et al., 2004, 2009), but they are either descriptive or regionally focused. There is a lack of studies quantifying how natural processes control pH globally. Here we assess the subsurface patterns in global climatological ocean pH, and determine the degree to which the pH distribution and its spatial variability are governed by anthropogenic changes, the advection of surface waters into the interior (the so-called preformed component), organic matter remineralization, and carbonate mineral (mostly $CaCO_3$, but also, e.g., $MgCO_3$) dissolution. The goal is to properly evaluate how anthropogenic changes and natural gradients collectively act on ocean pH and how this sets the regional vulnerability to future changes in ocean acidification.

2. Data and Methods

2.1. Data

Unless otherwise noted we use the Global Ocean Data Analysis Project version 2 (GLODAPv2) mapped climatologies (Lauvset et al., 2016) throughout this study, and all additional calculations are based on this product. The baseline value from which the various pH perturbations are estimated is pH^{2002}, which is calculated from the observed total alkalinity (TA) and dissolved inorganic carbon (DIC) in GLODAPv2 (Olsen et al., 2016), where DIC is first adjusted to year 2002 using the atmospheric perturbation method as detailed in Appendix B of Lauvset et al. (2016), and the assumption that TA does not change over time. Since few ship-based observations of ocean carbonate chemistry are made in winter there is a recognized seasonal bias in the GLODAPv2 data product (Olsen et al., 2019), and hence in all calculations made using these data, which makes the data product challenging to use for the surface ocean. No attempt has been made to correct for this bias in this present work, although we note that this bias is primarily an issue for surface measurements and this analysis focuses on the ocean interior. We nevertheless note that previous studies (e.g., Fassbender et al., 2018 ; Landschützer et al., 2018 ; Lenton et al., 2012) have indicated that there is a nonnegligible difference between summertime and wintertime trends in surface ocean pCO$_2$, and it is possible that this is also the case for pH. Therefore, the anthropogenic CO_2 impacts on pH (and Ω) estimated here, which align with previous estimates (e.g., Caldeira & Wickett, 2003), should be considered representative of the summertime. Relatedly, warming of the ocean also affects the amplitude of the seasonal cycling and ocean stratification, which has been shown to affect ocean pCO$_2$ (Fassbender et al., 2018; Landschützer et al., 2018). The same effect is likely for ocean acidification, but the GLODAPv2 data product, due to the seasonal bias, cannot be used to assess this effect. This effect has therefore not been accounted for or discussed in detail in this study.

All GLODAPv2 data are available for download through www.glodap.info. In this study, pH and pH changes are always on the total hydrogen scale and, unless otherwise stated, always calculated for in situ temperature and pressure.

2.2. Preformed Values

To estimate preformed total alkalinity (TA^0), we used a novel combination of the total matrix intercomparison (Gebbie & Huybers, 2011) and the Locally Interpolated Alkalinity Regression (LIARv2) methods (Carter et al., 2018). The approach used here is an evolution of the TA^0 estimate employed by Feely et al. (2002), which relied on basin-specific surface ocean regressions of TA with properties that are conserved in the interior ocean. It addresses two problems with the earlier approach: first, ocean interior ventilation tends to occur during the wintertime when seawater properties are substantially different (e.g., colder) than in the summer. Since the data used to train the regressions have mostly been collected during summer months, this can substantially bias the regressions toward that season, that is, conditions during winter, the time of water mass formation, is not well represented (Carter et al., 2014). Secondly, available TA regressions are valid for specific regions of the surface ocean, and since interior ocean water often originates from distant regions or other ocean basins entirely, selecting which regression to use is problematic. This new approach addresses these challenges by estimating seawater properties just below the shallow summer mixed layers and then propagating these estimates into the global ocean using the total matrix intercomparison approach (Gebbie & Huybers, 2011).

The total matrix intercomparison approach estimates—for a water parcel anywhere in the ocean interior—the fractions (f_i) of water from each of n total matrix intercomparison grid locations on the ocean surface that comprise the interior ocean mixture. The Locally Interpolated Regressions approach allows estimates that are specific to water masses just below each of the surface locations. Specifically, we use gridded interior ocean potential temperature (θ) and salinity (S) to estimate TA at 100-m depth at each of the n surface locations. Using the 100-m depth surface instead of the 0-m surface limits the impacts of seasonality on the measurements used to train the regressions (Pardo et al., 2011). These estimates now represent the characteristics of water ventilated from each of the n locations, or the TA^0 of each component water mass that collectively comprise the interior mixture. For each ocean interior location on our $1° \times 1° \times 33$ depth levels grid the n individual TA^0 estimates are weighted by f_i and then summed, to estimate the average TA^0 of the interior water parcel:

$$TA^0 = \sum_{i=1}^{n} f_i TA_i^0 \tag{1}$$

To visualize our new preformed alkalinity estimates (TA^0) we compare these values to the mapped TA in the GLODAPv2 data product (Lauvset et al., 2016; Figures S12 and S13). On the surface the difference is, as expected, very small (1 ± 20 μmol kg^{-1}, where the uncertainty is 1 standard deviation of the mean; Figure S11a) while it increases with depth to an average 103 ± 6 μmol kg^{-1} at 3,000 m in the North Pacific Ocean (Figures S12c and S14; uncertainty is 1 standard deviation of the mean) and water mass age (Figure S1), as a consequence of carbonate mineral dissolution.

2.3. Anthropogenic Carbon and Preindustrial Values

Anthropogenic carbon (C_{anth}) is calculated using the transit time distribution (TTD) method (Hall et al., 2002; Waugh et al., 2006) on all CFC-12 observations in GLODAPv2, following the method used by Lauvset et al. (2016), under the assumption that the ratio between the mean age and width of the TTD is unity ($\Gamma/\Delta = 1$). We used the TA^0 estimated as described in section 2.2 to calculate C_{anth} but note that the TTD based C_{anth} estimates are rather insensitive to how TA^0 is estimated (not shown). C_{anth} was normalized to year 2002 following the method outlined in Lauvset et al. (2016). Preindustrial pH (pH^{PI}), and aragonite (Ω_{Ar}^{PI}) and calcite saturation state (Ω_{Ca}^{PI}) are calculated in CO2SYS (Lewis & Wallace, 1998) version 2.0 for MatLab® (Orr et al., 2018; van Heuven et al., 2009) from DIC^{PI} and TA using the carbonate dissociation constants of Lueker et al. (2000), the bisulfate ion dissociation constant of Dickson (1990), the total borate-salinity relationship of Uppström (1974), and the mapped phosphate and silicate fields from GLODAPv2.

The TTD method used to estimate C_{anth} for this study is known to overestimate C_{anth} in the Southern Ocean due to the assumption of constant equilibrium (He et al., 2018; Khatiwala et al., 2013; Waugh et al., 2006). Waugh et al. (2006) suggests a 20% global overestimate in C_{anth} calculated using the TTD method, while Vazquez-Rodriguez et al. (2009) estimated that the TTD method overestimated C_{anth} in the Southern Ocean by 2–3 μmol kg^{-1} relative to the Sabine et al. (2004) inventory. As a result, the numbers presented here are likely slightly overestimated.

2.4. Decomposition of pH

In the ocean interior pH changes are (i) thermodynamically driven, primarily through changes in temperature (ΔpH^T) and pressure (ΔpH^{press}), and biogeochemically driven through (ii) net remineralization of organic carbon to inorganic carbon (ΔpH^{org}) and (iii) net dissolution of CaCO$_3$ minerals (ΔpH^{CaCO3}). The two latter processes do not directly change pH but rather add DIC or release TA (for carbonate dissolution) or titrate it away (for organic matter remineralization). These chemical changes then cause pH to change. In this paper, we consider the measured pH (pH^{2002}) to be the baseline and explicitly calculate how much the interior ocean pH is changed by each process, as well as the accumulation of anthropogenic carbon (ΔpH^{anth}). Our analysis is based on well-established methods that have been used to decompose DIC and TA in several previous studies (e.g.,Cameron et al., 2005 ; Couldrey et al., 2019 ; Eggleston & Galbraith, 2018 ; Gruber et al., 1996 ; Sarmiento & Gruber, 2006; Schmittner et al., 2013). In addition, a more simplified way to decompose interior ocean pH is detailed in Millero (2013), following Park (1969). All components were calculated in CO2SYS (Lewis & Wallace, 1998), using version 2.0 of CO2SYS for Matlab® (Orr et al.,
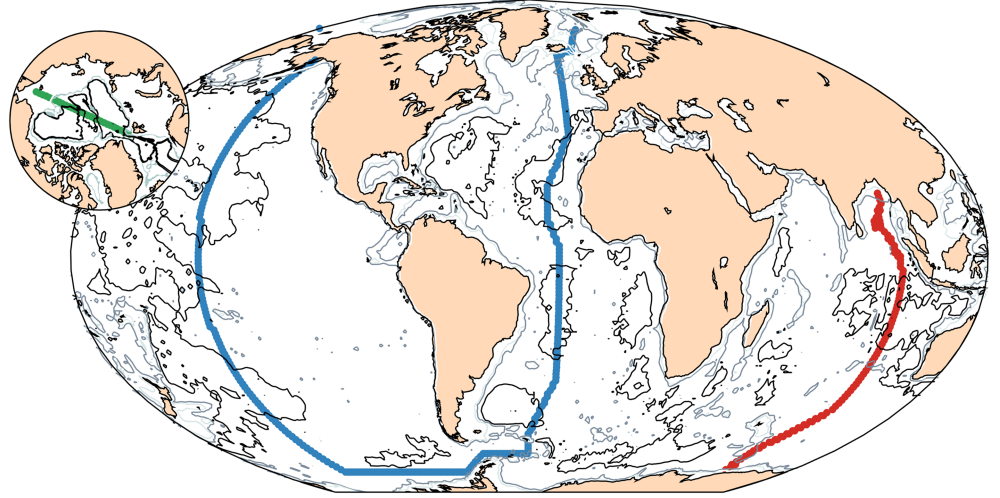
Figure 1. Map showing the three transects used to create the cross sections shown in Figures 2, 3, 5b, and 9. The blue transect begins in the Nordic Seas and then follows the GO-SHIP lines A16 southward in the Atlantic Ocean, SR04 and S04P westward in the Southern Ocean, and P16 northward in the Pacific Ocean. The red line follows the GO-SHIP line I09 southward in the Indian Ocean. The green line on the smaller inset crosses the Arctic Ocean from the Bering Strait to North Pole along 175°W and from the North Pole to the Fram Strait along 5°E.

2018; van Heuven et al., 2009), which includes routines for error propagation (Orr et al., 2018) used to estimate uncertainties for each component. The choice of dissociation constants is as described in section 2.3. Our results are visualized as cross sections for the four transects shown in Figure 1: (i) a line through the Nordic Seas along the zero meridian south to the Iceland-Shetland ridge; (ii) the Global Ocean Ship-based Hydrographic Program (GO-SHIP) lines A16 southward in the Atlantic Ocean, SR04 and S04P westward in the Southern Ocean, and P16 northward in the Pacific Ocean; (iii) the GO-SHIP line I09 southward in the Indian Ocean; and (iv) a line that crosses the Arctic Ocean from the Bering Strait to North Pole along 175°W and from the North Pole to the Fram Strait along 5°E. In addition, results are shown as global maps on three different depth horizons (20, 1,000, and 3,000 m).

Preformed preindustrial pH ($pH^{PI,0}$; at in situ temperature and surface pressure) is here interpreted as the preindustrial pH at time of water mass formation. Thus, it is estimated as pH after the impact of the above-mentioned processes have been removed from pH^{2002}:

$$pH_{P=0}^{PI,0} = pH^{2002} - \Delta pH^{CaCO3} - \Delta pH^{org} - \Delta pH^{press} - \Delta pH^{anth} \tag{2}$$

where pH^{2002} is the pH from GLODAPv2 normalized to year 2002 (see section 2.1), ΔpH^{CaCO3} represents the change in pH due to carbonate mineral cycling (equation (3)), ΔpH^{org} represents the change in pH due to organic matter remineralization (equation (4)), ΔpH^{press} represents change in pH due to changes in pressure (equation (5)), and ΔpH^{anth} represents the change in pH due to anthropogenic carbon accumulation (equation (6)).

$$\Delta pH^{CaCO3} = pH^{f(DIC,TA)} - pH^{f\left(DIC-DIC^{CaCO3}, TA-TA^{CaCO3}\right)} \tag{3}$$

$$\Delta pH^{org} = pH^{f\left(DIC-DIC^{CaCO3}, TA-TA^{CaCO3}\right)} - pH^{f\left(DIC-DIC^{CaCO3}-DIC^{org}, TA-TA^{CaCO3}-TA^{org}\right)} \tag{4}$$

$$\Delta pH^{press} = pH^{f(DIC,TA)} - pH_{P=0}^{f(DIC,TA)} \tag{5}$$

$$\Delta pH^{anth} = pH^{f(DIC,\ TA)} - pH^{f(DIC-C_{anth}, TA)} \tag{6}$$

where $pH^{f(DIC,TA)}$ is pH^{2002}. This calculation is identical to the used in the GLODAPv2 data product and is repeated in this study only to get the associated uncertainty estimate (see section 2.5). The added subscript P = 0 indicates that the calculation is performed at 0-dbar pressure. Quantifying the impacts of organic matter and carbonate mineral cycling require more steps. First, DIC^{org} and TA^{org} are defined as the dissolved

inorganic carbon and total alkalinity, respectively, accumulated at a location through the action of the soft tissue pump, or the remineralization of organic matter:

$$DIC^{org} = \frac{117 mol\, DIC}{170\, mol\, O_2} AOU \tag{7}$$

$$TA^{org} = -1.36 \frac{15.5 mol\, N}{170 mol\, O_2} AOU \tag{8}$$

where the stoichiometric ratios are those of Anderson and Sarmiento (1994); the 1.36 coefficient is from Wolf-Gladrow et al. (2007); and AOU, calculated using the Garcia and Gordon (1992) algorithm, is the apparent oxygen utilization, or the difference between the observed dissolved oxygen concentration and the oxygen concentration expected at gas exchange equilibrium (i.e., $O_2^{sat} - O_2^{obs}$). Second, DIC^{CaCO3} and TA^{CaCO3} are defined as the dissolved inorganic carbon and total alkalinity, respectively, accumulated at a location through the action of the hard tissue pump, that is, the net dissolution of carbonate minerals:

$$TA^{CaCO3} = TA - TA^0 - TA^{org} \tag{9}$$

$$DIC^{CaCO3} = \frac{1 mol\, DIC}{2 mol\, TA} \left[TA^{CaCO3} \right] \tag{10}$$

Third, TA^0 is estimated according to equation (1) while finally DIC^0 is calculated using equation (11):

$$DIC^0 = DIC^{2002} - DIC^{CaCO3} - DIC^{org} - C_{anth} \tag{11}$$

Preformed preindustrial pH (at in situ temperature and surface pressure) can be now be calculated either as pH^{2002} adjusted to remove the impacts of the processes considered (equation (2)) or as a function of the preformed preindustrial dissolved inorganic carbon and preformed total alkalinity:

$$pH_{P=0}^{PI,0} = pH^{f\left(DIC_{P=0}^{PI,0}, TA_{P=0}^0 \right)} \tag{12}$$

Note that ΔpH^{org} is calculated using DIC and TA adjusted for the amounts gained through $CaCO_3$ cycling (equation (3)) following Sarmiento and Gruber (2006) under the assumption that $CaCO_3$ dissolution happens after organic matter remineralization has changed both DIC and TA. This minimizes biases brought about by the nonlinear dependence of pH to DIC and/or TA perturbations.

As mentioned, all calculations are conducted at in situ temperature, under the assumption that this is conserved as water circulates through the interior ocean. Effects of hydrothermal heating and adiabatic expansion and compression of seawater are small and neglected. For example, the impact on pH of the heating water masses experience as they are transported from surface to higher pressures (adiabatic heating), is very small. Typically, a change of pressure from surface to 4,000 m generates a heating of about 0.4 °C, which would lead to a pH drop of ~0.006 units (as the pH change per 1 °C is ~0.015 under constant DIC and TA). The impacts of ocean mixing are captured in our preformed pH distributions (at in situ temperature). However, we caution that temperature plays a major role in driving the processes that lead to surface ocean variability in carbonate chemistry (Jiang et al., 2015) while only having a small net impact on the pH of surface waters that are well-equilibrated with the atmosphere (Jiang et al., 2019).

2.5. Uncertainty Analysis

The uncertainties in each input variable and parameter are listed in Table 1, and the error propagation equations for equations (3)–13 are given in equations S2–S15 in the supporting information. Following recommendations by Orr et al. (2018) these uncertainties are defined as standard uncertainties (1σ), and we assume that the uncertainties in DIC and TA are uncorrelated. Since we include the mapping error the assumption of uncorrelated uncertainties is not strictly true since where mapping error for DIC is large it is also large for TA. This leads to an overestimation of the overall uncertainty (Orr et al., 2018). Throughout the text and in all figures the final combined uncertainties (Figures S4–S8) are presented as 2σ. Some important caveats regarding our uncertainty analysis are detailed in the supporting information.

Table 1
Uncertainties in the Input Parameters Used in CO2SYS to Calculate pH and the Components of pH Given in equation (2)

| Input variable	Uncertainty (1σ)
σ (TA)[0]	5.5 µmol kg^{-1}[a]
σ (DIC)	Combination of measurement[b] uncertainty (4 µmol kg^{-1}) and spatially variable mapping[c] error summed in quadrature
σ (TA)	Combination of measurement[b] uncertainty (6 µmol kg^{-1}) and spatially variable mapping[c] error summed in quadrature
σ (salinity)	Combination of measurement[b] uncertainty (0.005) and spatially variable mapping[c] error summed in quadrature
σ (temperature)	The mapping error[c]
σ (phosphate)	Combination of measurement[b] uncertainty (2%) and spatially variable mapping[c] error summed in quadrature
σ (silicate)	Combination of measurement[b] uncertainty (2%) and spatially variable mapping[c] error summed in quadrature
σ (C_{anth})	Combination of estimation uncertainty (10%[d]) and the spatially variable mapping[c] error summed in quadrature
σ ($r_{C:O}$)	30%[e]
σ (AOU)	Combination of oxygen measurement[b] uncertainty (1%), spatially variable mapping[e] error, and uncertainty in oxygen saturation calculation[f]
σ (1.36 coefficient)	10%[g]
σ (pK_0)[h]	0.002
σ (pK_1)[h]	0.0075
σ (pK_2)[h]	0.015
σ (pK_b)[h,i]	0.01
σ (pK_w)[h,j]	0.01
σ (pK_{sp-a})[h,k]	0.02
σ (pK_{sp-c})[h,l]	0.02
σ (total boron)[h]	1%

[a]RMSE of TA from Table 1 in Carter et al. (2018). [b]Measurement uncertainties are taken from the GLODAPv2 (Olsen et al., 2016). We assume zero measurement uncertainty in temperature. [c]Mapping uncertainties are taken from the GLODAPv2 mapped data product (Lauvset et al., 2016). [d]Estimated based on the results of He et al. (2018). [e]Assumed based on range of published, commonly used stoichiometric ratios (e.g., Redfield et al., 1963; Takahashi et al., 1985; Li & Peng, 2002; Körtzinger et al., 2001). [f]0.3% following Garcia and Gordon (1992). [g]Estimated based on published values of this coefficient (Kanamori & Ikegami, 1982; Wolf-Gladrow et al., 2007). [h]Default uncertainty as given in the errors.m subroutine of the CO2SYS program (Orr et al., 2018). [i]Dissociation constant for boric acid. [j]Water dissociation constant. [k]Solubility product of aragonite. [l]Solubility product of calcite.

3. Results

3.1. pH Gradients Due to Natural Processes

Interior ocean pH^{2002} gradients are substantially larger than surface pH^{2002} gradients, with an in situ pH^{2002} range between 7.52 ± 0.05 and 8.33 ± 0.10 in the interior ocean (Figures 2a and S4). Mostly, this range is due to biological processes that affect the interior ocean pH as outlined in section 2.4, and pressure effects. Pressure has a significant impact on pH in the deep ocean interior, primarily due to the pressure effects on the dissociation constants for carbonic acid (K_1) and bicarbonate ion (K_2), and causes a decrease in pH with depth (Figure 3a). Along our section (Figure 1), which is never deeper than 5,500 m, ΔpH^{press} has a maximum impact of -0.27 ± 0.11, that is, the chemical speciation changes that result from increased pressure at depth decrease the pH in the deepest parts of our section by 0.27.
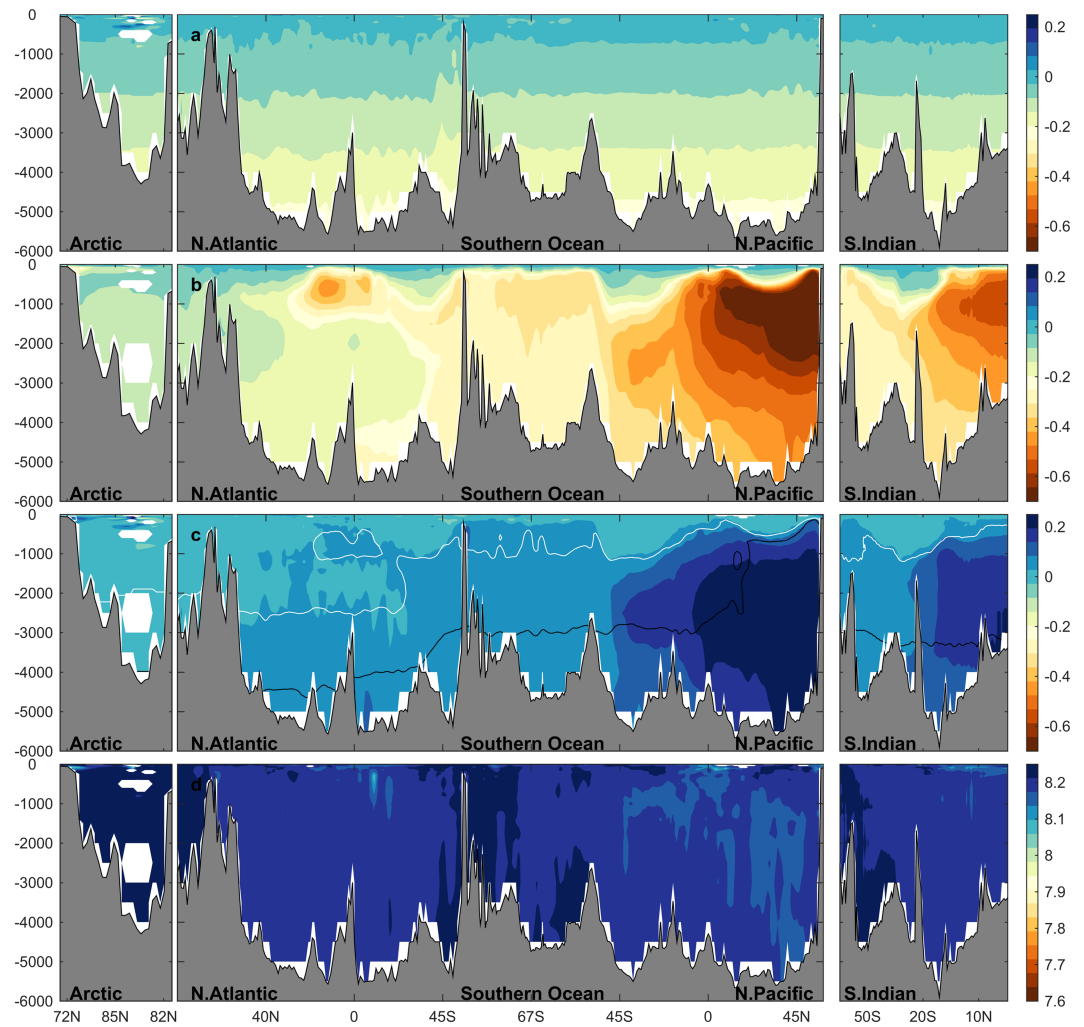
Organic matter remineralization leads to a decrease in interior ocean pH (Figure 3b) because remineralization increases the concentration of inorganic carbon. Of the four components that create the interior ocean pH gradients (equation (2)) ΔpH^{org} has the largest contribution overall, and has its largest impacts in the northern Pacific and the northern Indian Oceans where subthermocline water masses are typically older than 1,000 years (Figure S1): ΔpH^{org} is up to -0.79 ± 0.28 and -0.61 ± 0.23 in these regions, respectively (Figure 3b). As we use AOU to estimate organic matter remineralization there is naturally also a close correlation between maximum ΔpH^{org} and oxygen minimum zones, which are often not caused by high rates of organic matter remineralization, but rather lack of mixing and ventilation due to slow or stagnant circulation (Keeling et al., 2010). Along our transect, the spatial pattern ΔpH^{org} is also very similar to that in
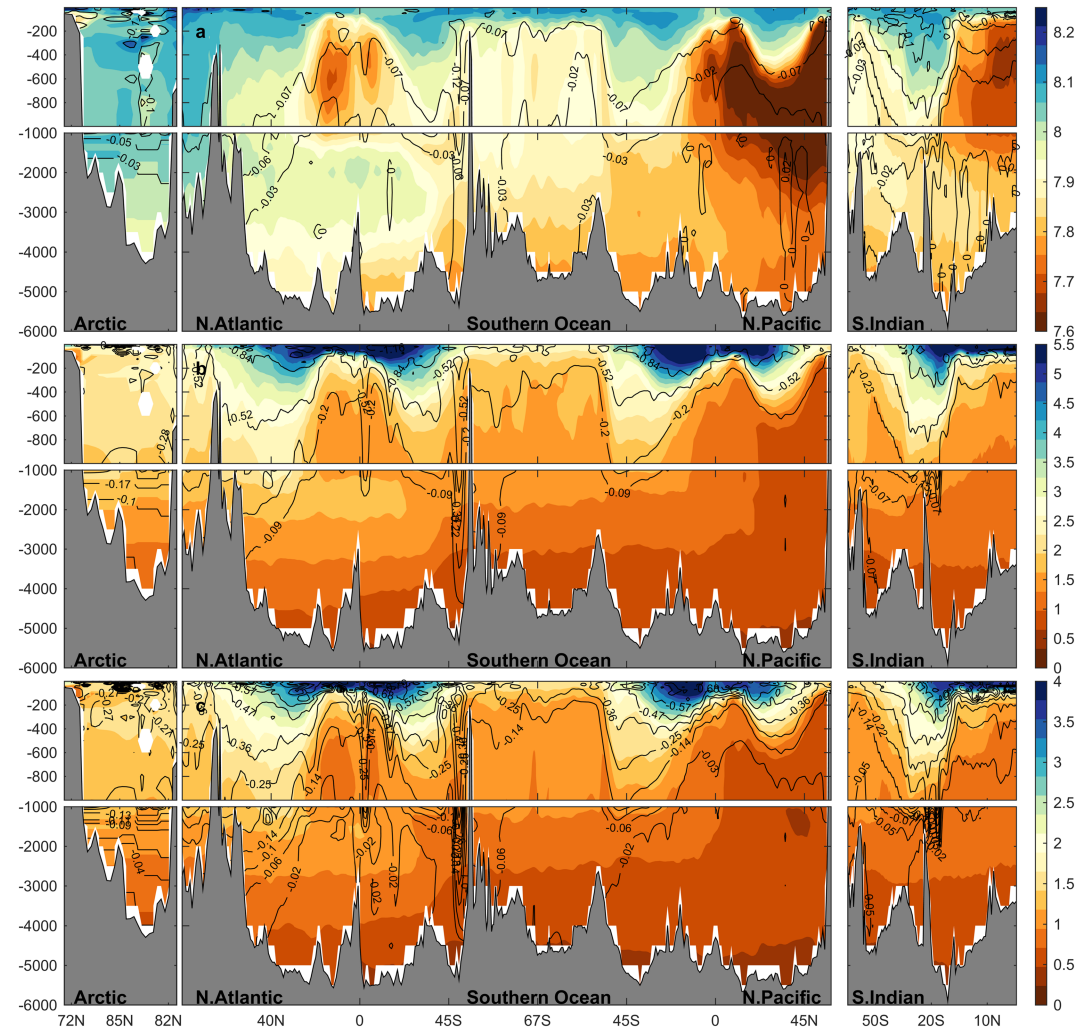
Figure 2. Vertical cross sections, along the transects shown in Figure 1, of (a) pH^{2002}, (b) Ω_{Ca}^{2002}, and (c) Ω_{Ar}^{2002}. All variables are reported for in situ temperature and pressure and are normalized to the year 2002 as in GLODAPv2 (Lauvset et al., 2016). pH is calculated on the total hydrogen ion scale. The black contours and numbers indicate the anthropogenic change from preindustrial to year 2002. Note the vertical scale change for the top 1,000 m. Regions where the mapping errors are unacceptable (Lauvset et al., 2016) are white. The vertical axis shows depth (m) below sea level.

both water mass age (Figure S1) and DIC^{org} (Figure S9) since the amount of remineralized carbon in seawater increases as the product of the age of the water mass and the average net rate of remineralization. That the age of the seawater is an important factor ($r = 0.65$) can clearly be seen in the steady decrease in the magnitude of ΔpH^{org} moving from south to north across the Pacific (Figure 3b). Both from the AOU (not shown) and the water mass age, the Southern Ocean (south of 45°S) appears quite recently ventilated, as expected due to active water mass formation in this region. Antarctic Intermediate Water and Subantarctic Mode Water are formed in the Antarctic Circumpolar Current, and spread northward to ventilate the Southern Hemisphere at ~1,000-m depth. These water masses show up with comparatively small ΔpH^{org} signals in all ocean basins (Figure 4b). There is nevertheless a significant subsurface ΔpH^{org} component (up to -0.37 ± 0.15) due to upwelling of quite old Pacific Deep Water and Upper Circumpolar Deep Water (Talley, 2013) near the polar front of the Antarctic Circumpolar Current (Figure 3b).

The importance of the rate of remineralization, approximated by dividing ΔpH^{org} by water mass age (Figures S10 and S11), can also be seen, for example, in the equatorial Atlantic where a ΔpH^{org} maximum is found in northward penetrating Antarctic Intermediate Water, which is younger than the North

Figure 3. Vertical cross sections, along the transects shown in Figure 1, of (a) the change in pH incurred by pressure changes (ΔpH^{press}; equation (5)), (b) the change in pH incurred by organic matter remineralization (ΔpH^{org}; equation (4)), (c) the change in pH incurred by the dissolution of $CaCO_3$ in the interior ocean (ΔpH^{CaCO3}; equation (3)), and (d) preformed preindustrial pH ($pH^{PI,0}_{P=0}$; equation 2) at surface pressure (0 dbar) and in situ temperature. Note that in (d) ΔpH^{anth} (Figure 5b) has also been removed. In (c) the white and black contour shows the depth where Ω_{Ca}^{2002} and Ω_{Ar}^{2002}, respectively, equal 1. Regions where the mapping errors are unacceptable (Lauvset et al., 2016) are white. The vertical axis shows depth (m) below sea level.

Atlantic Deep Water below it (Figures 4b and 4c), but shallower and subjected to higher rates of remineralization (Figures S11b and S11c). Local ΔpH^{org} maxima found in the upper 1,000 m of the ocean (Figures 3b and 4a–4c) are all associated with the thermocline or upwelling of older water and highlight that the largest vertical gradients in ΔpH^{org} are in the upper ocean, which is consistent with the Martin curve (Martin et al., 1987). Upwelling deep waters show up as patches of strong remineralization signals at 100 m on both sides of the equator in the Pacific, and along the U.S. western seaboard (Figure 4a). The deep ocean, on the other hand, generally has a very small, and spatially uniform, rates of remineralization (Figure S11c), but also here there are regional differences with well-ventilated areas generally having larger rates than old water masses. Related to this there is a clear inverse correlation ($r = -0.69$) between the rate of remineralization and C_{anth} (not shown).

In contrast to organic matter remineralization, $CaCO_3$ dissolution leads to an increase in pH (Figure 3c) because dissolution of $CaCO_3$ releases carbonate ions, thereby elevating TA more than DIC and increasing the buffer capacity (Feely et al., 2002, 2004, 2012; Zeebe & Wolf-Gladrow, 2001). Note that the spatial pattern in ΔpH^{CaCO3} closely resembles that of ΔDIC^{CaCO3} (see Sarmiento & Gruber, 2006, Figure 9.3.4), although
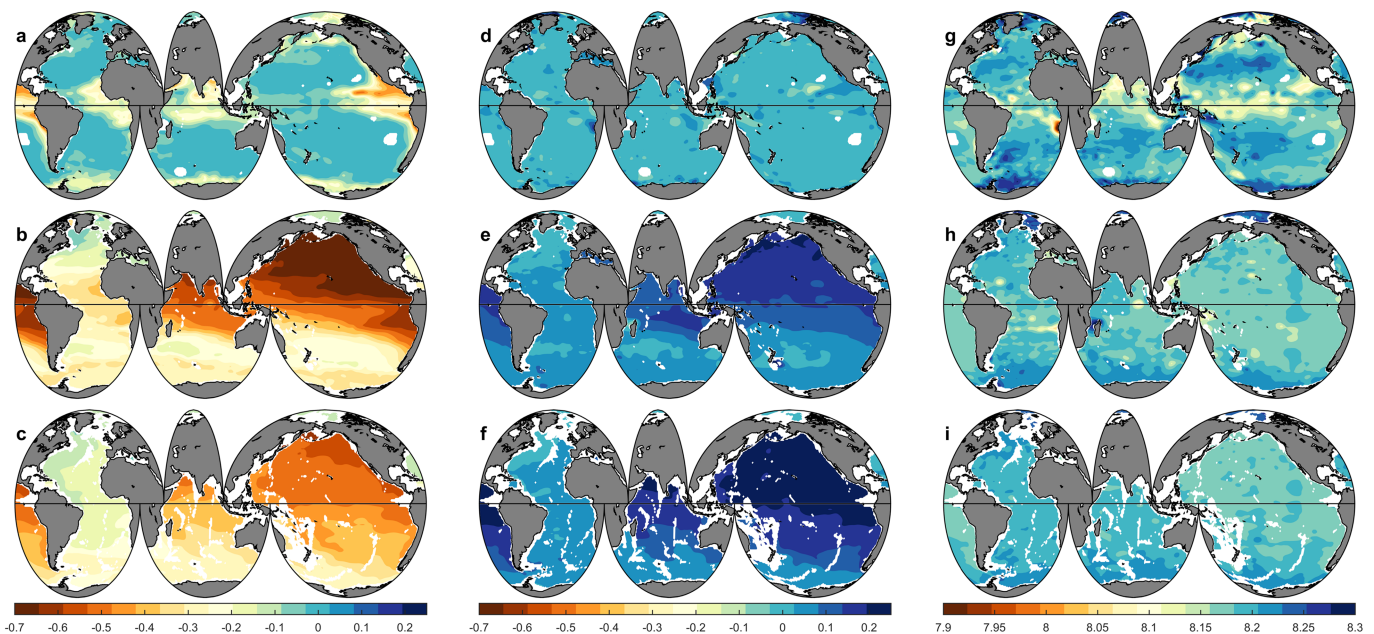
Figure 4. Maps of ΔpH^{org} (equation (4)) at (a) 100 m, (b) 1,000 m, and (c) 3,000 m; ΔpH^{CaCO3} (equation (3)) at (d) 100 m, (e) 1,000 m, and (f) 3,000 m; and $pH^{PI,0}_{P=0}$ (equation 2) at (g) 100 m, (h) 1,000 m, and (i) 3,000 m.

our maximum is somewhat shallower than that shown by Sarmiento and Gruber (2006). The impacts of carbonate mineral cycling are typically much smaller than the impacts of organic matter cycling both because more carbon is cycled as organic matter than as carbonate minerals and because the effects on pH of increased TA (2 per $CaCO_3$ dissolved) are partially offset by the effects of increased DIC (1 per $CaCO_3$ dissolved). Interior ocean net carbonate dissolution lead to an increase in pH of at most 0.24 ± 0.12 in the North Pacific, and 0.22 ± 0.10 in the northern Indian Ocean. In both these regions, the maximum impact is centered around 2,500 m. In the North Pacific, the calcite saturation horizon is very shallow (200–700 m), although still approximately 100–300 m deeper than the aragonite saturation horizon (Figure 3c), which is consistent with previous studies (Feely et al., 2002, 2012). Though well-known and much described, the shallow and similar depths for aragonite and calcite saturation horizons are unusual since everywhere else the calcite saturation horizon is deeper than 3,000 m, and ~2,000 m deeper than the aragonite saturation horizon. This pattern is ultimately governed by the remineralization of organic matter, the DIC accumulation in the oldest water masses leads to greater decreases in pH—as discussed above—and corrosive conditions for calcite and aragonite. The global pattern of ΔpH^{CaCO3} therefore resembles the pattern of ΔpH^{org}, but with an opposite sign and reduced magnitude for reasons mentioned above. Interestingly, the area of high ΔpH^{CaCO3} found in the northern Indian Ocean does not have a corresponding shallow calcite saturation horizon, as found in the North Pacific, but the aragonite saturation horizon does shoal toward the surface.

Distributions of $pH^{PI,0}_{P=0}$, the preindustrial pH at time of water mass formation, which are subsequently only changed by mixing in the interior ocean, are displayed in Figures 3d and 4g–4i. $pH^{PI,0}_{P=0}$ is highly homogeneous in the ocean interior with an average of 8.20 ± 0.14 at both 1,000 and 3,000 m (Figures 4h and 4i). Given the sensitivity of pH to temperature, and the relatively large temperature gradients near the surface (i.e., at 100 m), the surface gradients in $pH^{PI,0}_{P=0}$ are large (Figure 4g). However, below 1,000 m $pH^{PI,0}_{P=0}$ is 8.20 ± 0.13 throughout the transects chosen here (Figure 3d). This indicates that the major natural processes, which add or remove DIC and TA in the ocean interior and thus change pH, have been accounted for and quantified fairly accurately. As an additional control for the validity of our decomposition we use the estimated TA^0 (equation (1)) and $DIC^{PI,0}$ (equation (11)) to calculate preformed preindustrial partial pressure of CO_2 ($pCO_2^{PI,0}$; Figure S14). Given that $DIC^{PI,0}$ accumulates all sources of error, it lends confidence in our preformed properties, and thus our decomposition, that the difference between our $pCO_2^{PI,0}$ estimate and the approximate preindustrial atmospheric CO_2 ($xCO_2^{PI,atm}$ ~280 ppm) is consistent with
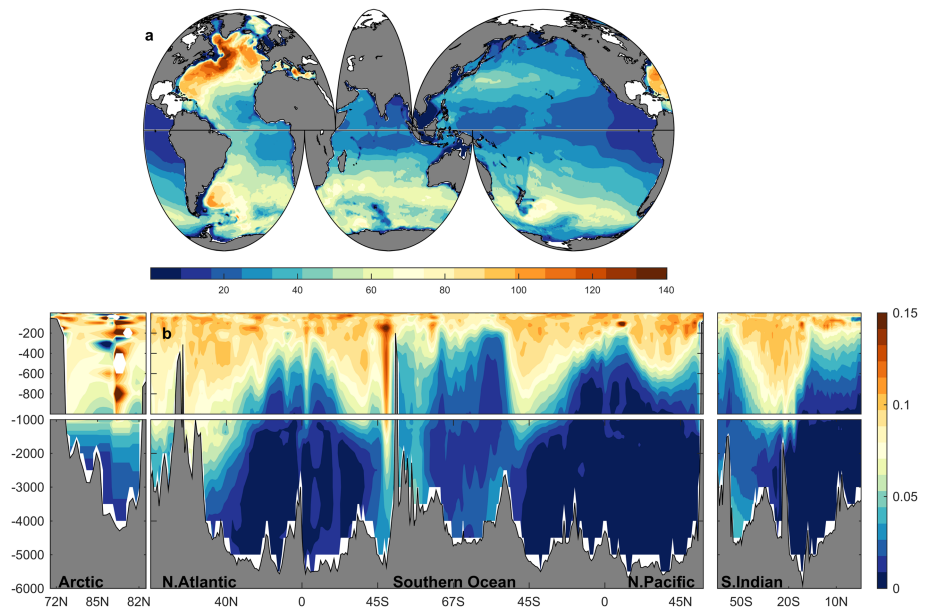
Figure 5. (a) Column inventories of anthropogenic carbon (mol C m^{-2}) in year 2002. (b) Vertical cross sections, along the transects shown in Figure 1, of ΔpH$^{\text{anth}}$ (equation (6)). The vertical axis shows depth (m) below sea level.

theoretical expectations in having higher undersaturation signals in the high latitudes compared to the lower latitudes. Note that nowhere is our pCO$_2$$^{\text{PI,0}}$ significantly different from xCO$_2$$^{\text{PI,atm}}$.

3.2. Anthropogenic Changes

The anthropogenic change in ocean pH is due to the ocean's increasing absorption of CO$_2$ from the atmosphere. This uptake is driven by the increasing partial pressure of CO$_2$ in the atmosphere and has led to more carbon being stored in the ocean. The estimates of the impact of anthropogenic CO$_2$ changes on pH (Figure 5b) reaffirm the large and well-understood anthropogenic impact on pH in the surface ocean (Jiang et al., 2019), and put it in the context of natural pH gradients in the interior ocean. In the top 200 m ΔpH$^{\text{anth}}$ is >80% of ΔpH$^{\text{org}}$, and in the convergence zones ΔpH$^{\text{anth}}$ is at least 40% of ΔpH$^{\text{org}}$ down to 800 m. Along the section shown here, the 0.05 ΔpH$^{\text{anth}}$ contour only extend deeper than 1,000 m in the North Atlantic, Arctic, and parts of the Southern Ocean (Figures 2a and 5b)—regions where the water column inventory of C$_{\text{anth}}$ (Figure 5a) is large. Thus, 1,000 m is generally the depth below which natural gradients dominate and anthropogenic changes are small.

This paper focuses mainly on interior ocean carbonate chemistry gradients, but it is important to consider surface ocean changes for context and because anthropogenic changes in pH originate at the surface. Surface ocean pH is clearly lower in year 2002 than it was in preindustrial times (Figures 6a and 6b). The decrease in surface waters is a globally quite uniform 0.10 ± 0.10 (Figure 6c and see Text S3 in the supporting information for notes on the uncertainty), although the uncertainty is spatially more variable than the change itself (Figure S7c). Since the pH scale is logarithmic this change represents a 25% increase in surface ocean acidity (total hydrogen ion concentration) relative to preindustrial times (approximately year 1800). The Intergovernmental Panel on Climate Change estimates 26% increased total hydrogen ion concentration since 1850 (IPCC, 2013), which, given the uncertainties, is indistinguishable. Corresponding to the change in DIC and pH the surface ocean saturation states of both aragonite (Ω_{Ar}; Figures 2b and 6d–6f) and calcite (Ω_{Ca}; Figures 2c and 6g–6i) have also decreased since preindustrial times, by on average -0.53 ± 0.71 and -0.81 ± 1.10, respectively (where the uncertainties are the average of the 2σ shown in Figures S8f and S8j).

4. Discussion

4.1. Anthropogenic Change and Its Drivers

Anthropogenic ocean pH changes are a direct function of the accumulation of C$_{\text{anth}}$ in the ocean so any quantification of ΔpH$^{\text{anth}}$ depends to some degree on how C$_{\text{anth}}$ is estimated. In this study we use the
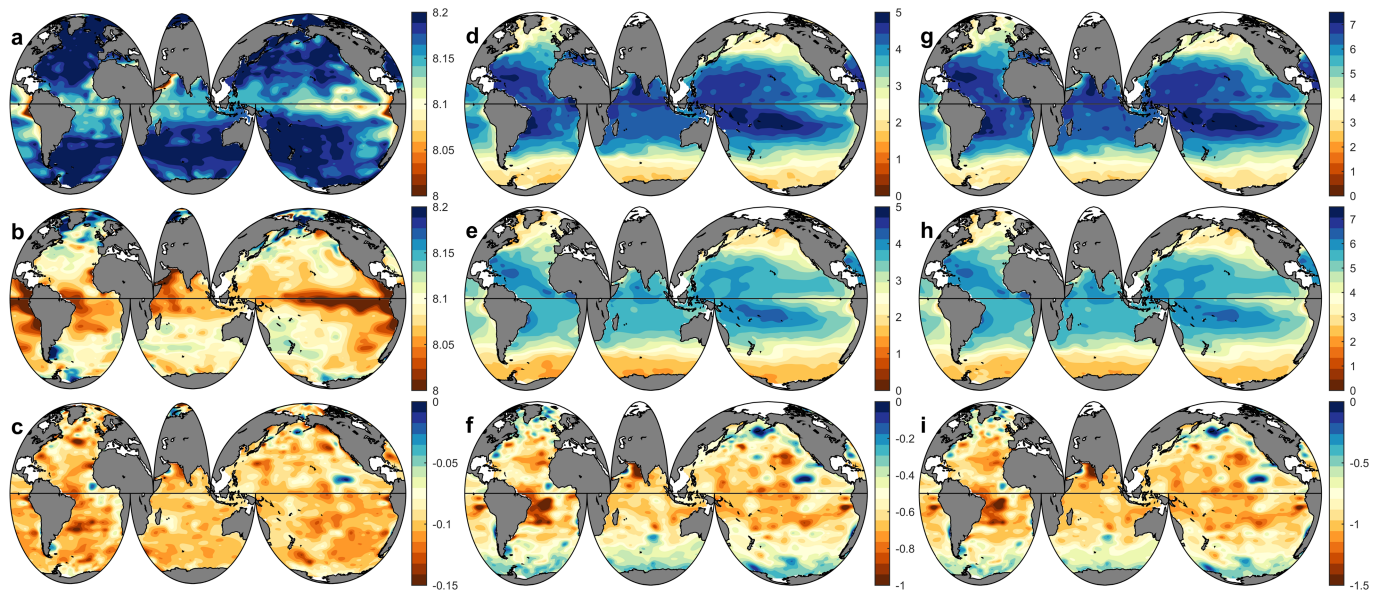
Figure 6. Global surface (20 m) map of (a) preindustrial pH, (b) pH^{2002}, (c) ΔpH^{anth} (equation (6)), (d) preindustrial Ω_{Ar}, (e) Ω_{Ar}^{2002}, (f) $\mathbf{\Delta\Omega_{Ar}}^{anth}$ ($=\Omega_{Ar}^{2002} - \Omega_{Ar}^{PI}$), (g) preindustrial Ω_{Ca}, (h) Ω_{Ca}^{2002}, and (i) $\mathbf{\Delta\Omega_{Ca}}^{anth}$ ($=\Omega_{Ca}^{2002} - \Omega_{Ca}^{PI}$).

TTD method (see section 2.3) and the estimated water column inventory of C_{anth} (Figure 5a) of 167 ± 29 PgC is (just) within the uncertainties of the estimate by Khatiwala et al. (2013) for 2010 (155 ± 31 PgC) and the more recent of estimate of 160 ± 20 PgC for 2010 by Gruber et al. (2019) based on the eMLR(C*) approach (Clement & Gruber, 2018). Our estimate is for an earlier year (2002) and yet is the highest of the three, but regardless, the comparability with previous estimates, along with the spatial pattern being consistent with previous work (e.g.,Khatiwala et al., 2013 ; Sabine et al., 2004), lends confidence to the estimates of the impact of anthropogenic CO_2 on pH presented here.

Ocean pH is changing as a direct response to accumulation of C_{anth}, but the magnitude of pH change for a given change in DIC ($\partial pH/\partial DIC$) is dependent on how much DIC and TA are present (Figure 7). Near the surface, $\partial pH/\partial DIC$ is smaller than at depth, meaning that a surface change in C_{anth} will lead to a smaller change in pH than a deep change. Figure 8a, comparing the ΔpH^{anth} with the accumulated C_{anth}, shows that the change in pH for any given C_{anth} concentration is larger (-0.0026 ± 0.000013 pH units per µmol kg^{-1} C_{anth} (where the uncertainty is the 95% confidence interval around the slope)) when C_{anth} is low (<40 µmol kg^{-1}), than where C_{anth} is high. This reflects that the DIC/TA ratios, and thus $\partial pH/\partial DIC$, are largest in the deep ocean where the anthropogenic carbon concentrations are low. There is a similar difference when looking only at the surface waters (i.e., where C_{anth} is high) with larger $\partial pH/\partial DIC$ in cold water than in warm water (compare Arctic and Tropics in Figure 7). For Ω_{Ar}, on the other hand, there is no apparent breakpoint in the rate of change with C_{anth} (Figure 8b) which is because the sensitivity of a change in Ω_{Ar} for a given change in DIC ($\partial\Omega_{Ar}/\partial DIC$) is strongest at the surface and in warm water (Figure S17). The relationship visualized in Figure 7 highlights that anthropogenic changes happens on top of a natural gradient, and that the size of this gradient will influence ΔpH^{anth}, both on the surface and in the interior ocean. To assess how the natural processes affect the anthropogenic impacts we calculate pH_{no-nat}^{anth} from the preformed values (equation (14)) and compare that with the outcome of equation (6). The subscript "no nat" here indicates that the natural processes have been removed.
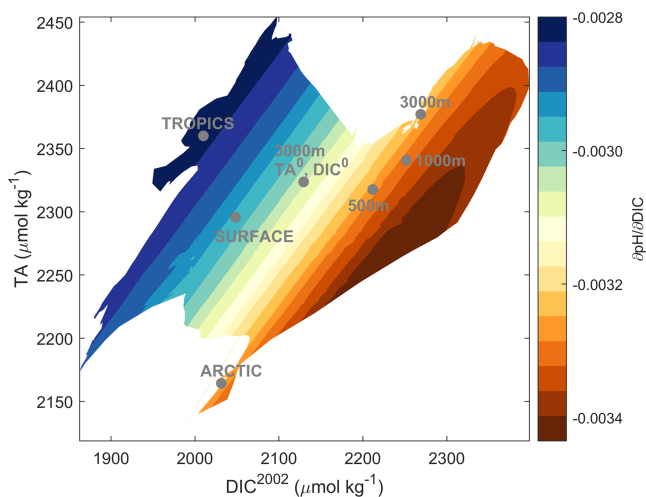
Figure 7. Visualization of the sensitivity of change in pH for a given change in DIC ($\partial pH/\partial DIC$) as a function of DIC and TA. $\partial pH/\partial DIC$ is calculated from the GLODAPv2 data using the derivnum function. This function is part of the CO2SYS software, and has been modified here to output pH (rather than H+). Note that the sensitivity has been calculated for surface pressure (0 dbar) and 25 °C in order to visualize the effects of DIC and TA only.
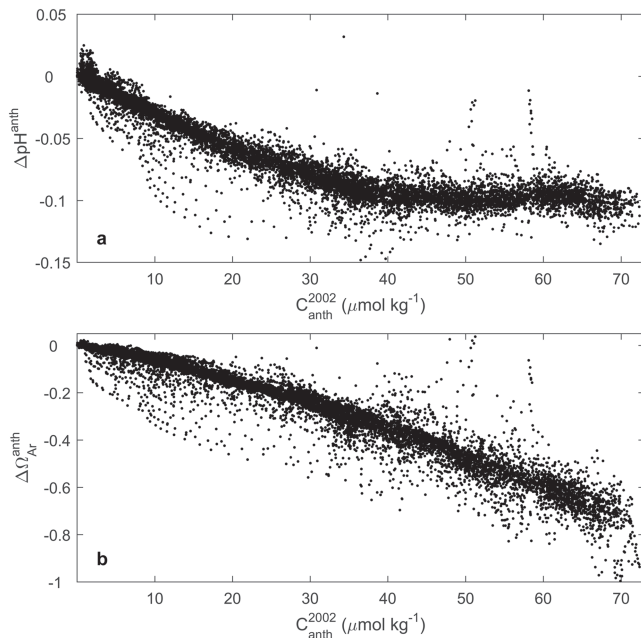
Figure 8. Scatterplot showing (a) ΔpH^{anth} relative to C_{anth} content in 2002 and (b) $\Delta \Omega_{Ar}^{anth}$ relative to C_{anth} content in 2002. The rates of change are estimated using linear regressions with a breakpoint at 40 $\mu mol\ kg^{-1}$ C_{anth}.

$$pH_{no\text{-}nat}^{anth} = pH^{f\left(DIC^{PI,0}+C_{anth},TA^0\right)} - pH^{f\left(DIC^{PI,0},TA^0\right)} \qquad (14)$$

The difference between ΔpH^{anth} and $pH_{no\text{-}nat}^{anth}$ is presented in Figure 9. Clearly, the inclusion of DIC from the remineralization of organic matter (DIC^{org}) in the estimate gives a greater pH change for any given increase in C_{anth}. This result reflects the changing $\partial pH/\partial DIC$ as water circulates in the deep ocean and accumulate DIC^{org}: C_{anth} is added to the ocean at the surface, water then sinks out of the surface, DIC^{org} is added as the waters circulate in the deep ocean, $\partial pH/\partial DIC$ increases because of the increased DIC, and the increased sensitivity leads to a strengthening of the the initial pH decline brought about by the uptake of C_{anth} at the surface. Note that comparing equations (6) and (14) does not directly tell us how much more sensitive pH is to addition of DIC^{org}, which would have to be quantified by modifying equation (4), only how much the initial acidification is increased when remineralization subsequently happens. Increased TA from carbonate mineral dissolution, the other natural process discussed in this paper, would be expected to decrease $\partial pH/\partial DIC$ and thereby reduce the pH change due to addition of C_{anth}, but these chemical changes are more than compensated by the release of CO_2 through organic matter remineralization, which is clearly seen when comparing $\partial pH/\partial DIC$ at 3,000 m in an ocean without biology (labelled 3,000 m; TA^0, DIC^0 in Figure 7) and $\partial pH/\partial DIC$ at 3,000 m in an ocean with biology (labelled 3,000 m in Figure 7). Hereafter we refer to the strengthened ΔpH^{anth} due to the addition of DIC^{org} as an enhancement.

We find that in the depth layer 500–1,500 m the net enhancement is on average 28 ± 15% along our section, but there are large regional and vertical gradients (Figure 9). In the deep ocean, except in the Southern Ocean, the differences between $pH_{no\text{-}nat}^{anth}$ and ΔpH^{anth} are generally very small (<0.005; Figure 9a) and have therefore been removed from further analysis (Figure 9b). In the Southern Ocean there is a significant amount of C_{anth} at the bottom, and here the ocean acidification enhancement decreases from 71 ± 4% in the 800–1,500-m range to 25 ± 4% deeper than 4,000 m. In the upper ocean (<1,500 m), however, the largest enhancements are found in low-oxygen regions like the equatorial Atlantic where the difference is 48 ± 13%. In the Indian Ocean the strongest enhancement (70 ± 10%) is found between 1,200 and 1,750 m just north of
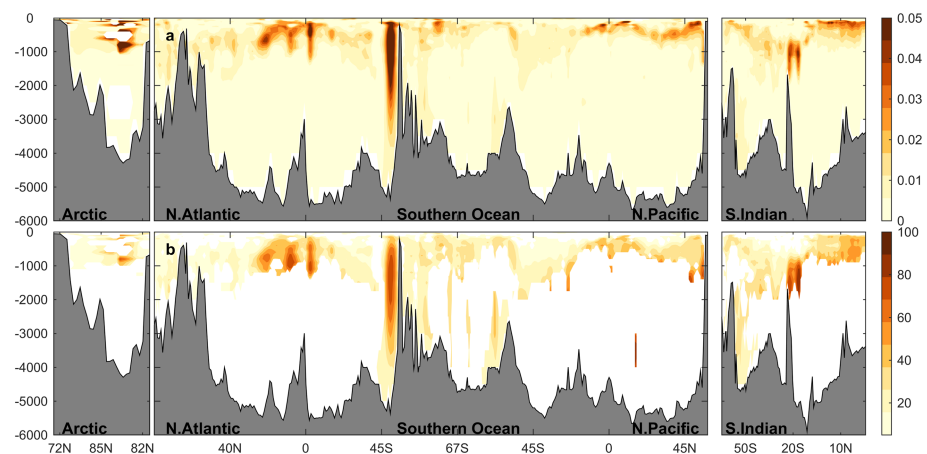
Figure 9. (a) Vertical cross sections showing the difference between anthropogenic pH change (equation (6)) and the same when the natural processes are removed first (equation (14)). (b) Vertical cross section showing the relative difference between equations (6) and (14), that is, (equations (6)–(14))/equation (6), presented as a percent change. Note that everywhere the numerator is less than 0.005 has been removed. This is because the denominator is also generally very small in these areas and this creates misleadingly large enhancement. The vertical axis shows depth (m) below sea level.

the Broken Plateau, where high AOU corresponds with the shoaling of the aragonite saturation horizon. In the Pacific Ocean the maximum along our section is $35 \pm 14\%$ at 300–1,750 m. While these relative changes appear large, the largest relative enhancements are found in areas of low oxygen that tend to have low concentrations of C_{anth}. However, as C_{anth} continues to be added to the ocean and propagate into poorly ventilated portions of the ocean this enhancement will grow more pronounced. In this regard the regional patterns are important to quantify as they render some ecosystems more vulnerable than others.

4.2. Ecosystem Vulnerabilities

Research is ongoing as to at what point the decrease in pH, Ω_{Ar}, and Ω_{Ca} will exceed ecosystems' natural thresholds for sustainability. In that respect, it is interesting that a recent study (Sulpis et al., 2018) found that there is already an observable anthropogenically induced $CaCO_3$ dissolution at the ocean bottom in the North Atlantic, where deep-sea corals persist in comparatively high-pH deep waters with little naturally accumulated carbon from organic matter remineralization. By contrast, in the North Pacific Ocean pH is naturally low because of the strong effect of organic matter remineralization which is only partially compensated by $CaCO_3$ dissolution. The northern North Pacific also has a very shallow aragonite saturation horizon (<200 m in some places). Thus, despite the anthropogenic impact overall being smaller in the North Pacific compared to the North Atlantic, it is possible that Pacific ecosystems are more vulnerable to ocean acidification because the changes compound on naturally low pH; that is, they are already close to $CaCO_3$ undersaturation. However, assessing the impact of ocean acidification on marine organisms is difficult since the impacts are often species specific and regionally varying (e.g.,Fabry et al., 2008 ; Gattuso et al., 2015 ; Kroeker et al., 2013), but what is clear is that heavily calcified organisms are particularly sensitive, while organisms that are able to move themselves have higher tolerances (Kroeker et al., 2013). It has been shown that it is the $CaCO_3$ saturation state rather than $[CO_3^{2-}]$ or pH which controls calcification (e.g.,Bednaršek et al., 2017; Fabry et al., 2008; Osborne et al., 2019; Waldbusser et al., 2015), and recent research from the North Pacific indicate that some calcifying species are quite vulnerable to anthropogenic change (Bednaršek et al., 2014, 2016, 2017, 2018; Feely et al., 2016; Osborne et al., 2019). Other studies (e.g., Fabry et al., 2008) have found that organisms adapted to strong natural gradients in carbonate chemistry have better mechanisms for buffering such variations, but it is still unclear whether this means they are also more resilient to anthropogenic changes that shift the natural gradient toward lower pH and shallower saturation horizons. Furthermore, naturally low-pH, high-DIC waters have a higher $\partial pH/\partial DIC$ and are thus more sensitive to further C_{anth} accumulation (Figures 7–9). In the Southern Ocean, a region sensitive to anthropogenic changes due to the natural shallow minimum in (CO_3^{2-}), a recent model study (Negrete-García et al., 2019) shows that there is a high likelihood of a very rapid emergence of shallow (<100 m) saturation horizon for aragonite, largely due to the accumulation of CO_2 in the thermocline, which decreases the natural minimum in $[CO_3^{2-}]$ enough to cause undersaturation.

While this paper focuses on pH in the interior ocean the anthropogenic change is largest at the surface; thus, any ecosystem impact is likely to first be seen there. As an example application of the quantified anthropogenic changes in pH and Ω presented in this study we have estimated the potential loss of suitable habitat for shallow calcifying corals. In today's ocean coral reef ecosystems do not thrive where the water has $\Omega_{Ar} < 3$ (Guinotte et al., 2003), and Figure 10 shows the extent of the ocean areas with surface $\Omega_{Ar} \geq 3$ in 2002 (Figure 10a) and in preindustrial times (Figure 10b). The potential habitat loss, defined as the preindustrial area minus the area in 2002, is 35,300,000 km^2. The calculation uncertainty for Ω_{Ar} is substantial, largely due to the large uncertainty in the solubility product (Orr et al., 2018). Thus, the smallest possible extent in preindustrial times approximately equals the largest possible extent in 2002 and the uncertainty in the loss of area (ranging from 35,000,000 to 83,000,000 km^2) is very large. Regardless of the change in habitat with $\Omega_{Ar} \geq 3$ an interesting feature in Figure 10 is that there are large regions today which appear to be very vulnerable to further anthropogenic changes. If the minimum 2002 area is used then the South China Sea and the East Indian Archipelago as well as most of the west coast of the Americas all have $\Omega_{Ar} < 3$. If the maximum area is used, these regions mostly have $\Omega_{Ar} > 3$, but the fact that just the uncertainty in the global mapped Ω_{Ar} yield such large differences indicate that these regions are just within the "healthy" zone and thus particularly vulnerable to additional anthropogenic changes. The above estimate of area loss, calculated using the best available observations of ocean carbonate chemistry, highlights the need for reducing the
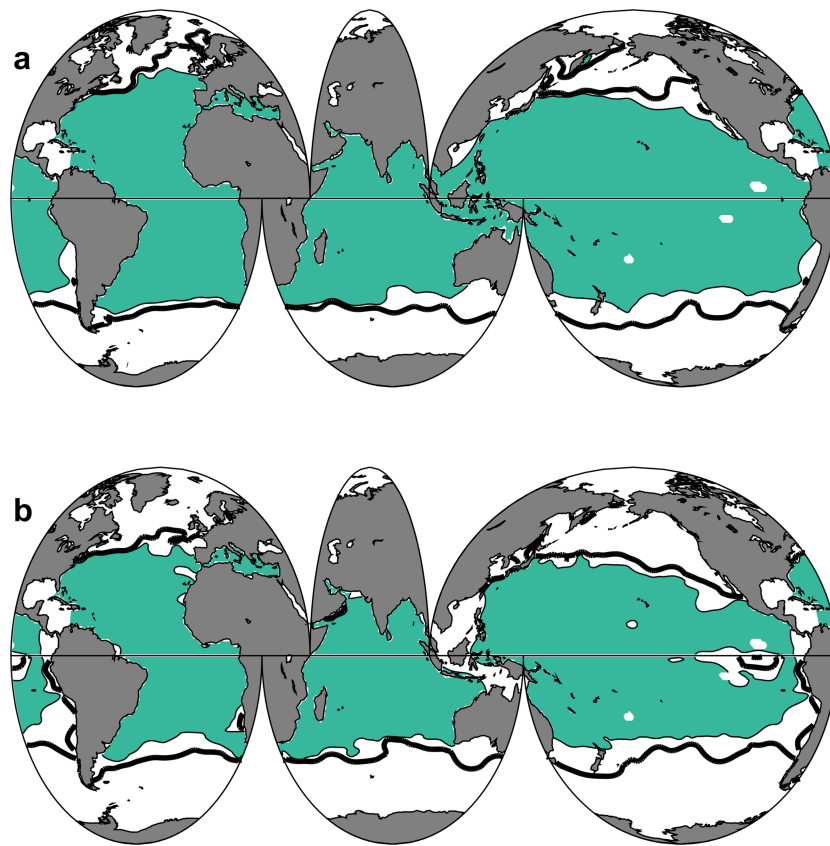
Figure 10. Map showing surface ocean area where $\Omega_{Ar} \geq 3$ (0 m). The black contour indicates maximum extent and the green area the minimum extent. (a) Preindustrial extent and (b) extent in 2002. The minimum and minimum extents are calculated using $\Omega_{Ar} \pm \sigma (\Omega_{Ar})$, where $\sigma (\Omega_{Ar})$ is the combination of the calculation uncertainty and the mapping error summed in quadrature.

uncertainty in both observations and calculations. Until then, fully quantifying the environmental stress all ocean ecosystems are subject to, both today and in the future, remain difficult.

4.3. Caveats

There are some notable caveats regarding possible sources of bias in our study. First, it is clear from much previous work that $pH^{PI,0}_{P = 0}$ is sensitive to how DIC^{org} and TA^{org} are calculated. AOU, which is used in our study, is the most commonly used method because it does not require knowledge about preformed values. However, previous studies (e.g., Carter et al., 2014; Ito et al., 2004; Talley et al., 2003; Russell & Dickson, 2003) have raised questions about the appropriateness of AOU as a proxy for organic matter remineralization given the assumption that a water mass is fully saturated with atmospheric oxygen at the time of subduction. This has for a long time been known to be incorrect (e.g., Redfield et al., 1963) since the degree to which saturation is reached depends on many factors including, but not limited to, wind speed, cooling, ice cover, and biological processes on the surface (e.g., Duteil et al., 2012). In addition, the use of AOU as a proxy for organic matter remineralization does not account for the fraction that occurs through denitrification. Deutsch et al. (2001) estimated the impacts of water column denitrification in the North Pacific, finding a maximum nitrate loss in oxygen-deficient zones of ~10 μmol kg^{-1}, which implies that our AOU-based DIC^{org} is off by a comparable number. Denitrification can therefore be assumed to result in a ΔpH^{org} estimate error of ~0.03 within oxygen-deficient zones and considerably less elsewhere. Second, constant stoichiometric ratios have been used throughout this study, while there is ample evidence that these ratios vary both spatially and temporally (e.g., Arrigo et al., 1999; Frigstad et al., 2011; Geider & La Roche, 2002; Li & Peng, 2002). However, as discussed in Deutsch and Weber (2012), synthesis efforts show that there appears to be a global mean stoichiometry similar to the classical Redfield ratio. Using spatially varying stoichiometry would likely change the results presented here, so we conservatively assume a 30% uncertainty

applied to our globally uniform $r_{C:O}$ value (Table 1) to account for the possible latitudinal range of variability in stoichiometric ratios.

5. Summary and Conclusions

We decompose pH into components describing the anthropogenic impact (ΔpH^{anth}), organic matter remineralization (ΔpH^{org}), $CaCO_3$ cycling (ΔpH^{CaCO3}), thermodynamics (ΔpH^T and ΔpH^{press}), and ocean circulation ($pH^{PI,0}_{P=0}$). The ΔpH^{org} component is the most important (maximum reduction of 0.79 ± 0.26) in explaining the interior ocean pH gradients, while ΔpH^{CaCO3} has a significant effect only at quite large depths (centered around 2,500 m) in the North Pacific and the northern Indian Oceans. The Atlantic Ocean sector of the Southern Ocean, which has a naturally shallow aragonite saturation horizon, is one area where the gradient between the surface ocean pH (~8.2) and the naturally low subsurface pH (~7.9) is quickly vanishing due to invasion of anthropogenic carbon. Here pH is naturally low due to strong organic matter remineralization, and anthropogenic changes are penetrating very deep (ΔpH^{anth} ~0.07 at 1,000 m), and this is an area recently identified as being particularly sensitive to small changes in ocean carbonate chemistry (Negrete-García et al., 2019). When removing the organic matter remineralization and $CaCO_3$ cycling from the estimate ΔpH^{anth} becomes smaller, indicating an enhancement of anthropogenic pH changes by natural processes, which is likely to continue and grow stronger as ocean acidification continues. With the exception of the Southern Ocean, we currently see this enhancement only in the upper ocean (<1,500 m) and most pronounced in low-oxygen areas. Anthropogenic emissions of CO_2 have led to both decreased pH and decreases in the saturation states of $CaCO_3$ minerals. However, given the uncertainties in calculating the ocean carbonate chemistry it is difficult to conclude definitively how large this impact is on ocean ecosystems. Thus, fully quantifying the environmental stress ocean ecosystems are subject to both today and in the future through the reduction of uncertainty in the observations and calculations remains a priority.

References

Anderson, L. A., & Sarmiento, J. L. (1994). Redfield ratios of remineralization determined by nutrient data-analysis. *Global Biogeochemical Cycles*, 8(1), 65–80.

Arrigo, K. R., Robinson, D. H., Worthen, D. L., Dunbar, R. B., DiTullio, G. R., VanWoert, M., & Lizotte, M. P. (1999). Phytoplankton community structure and the drawdown of nutrients and CO_2 in the Southern Ocean. *Science*, 283(5400), 365–367. https://doi.org/10.1126/science.283.5400.365

Bates, N., Astor, Y., Church, M., Currie, K., Dore, J., Gonaález-Dávila, M., et al. (2014). A time-series view of changing ocean chemistry due to ocean uptake of anthropogenic CO_2 and ocean acidification. *Oceanography*, 27(1), 126–141.

Bednaršek, N., Feely, R. A., Beck, M. W., Glippa, O., Kanerva, M., & Engström-Öst, J. (2018). El Niño-related thermal stress coupled with upwelling-related ocean acidification negatively impacts cellular to population-level responses in pteropods along the California Current System with implications for increased bioenergetic costs. *Frontiers in Marine Science*. https://doi.org/10.3389/fmars.2018.00486

Bednaršek, N., Feely, R. A., Reum, J. C. P., Peterson, W., Menkel, J., Alin, S. R., & Hales, B. (2014). Limacina helicina shell dissolution as an indicator of declining habitat suitability due to ocean acidification in the California Current Ecosystem. *Proceedings of the Royal Society B: Biological Sciences*, 281(1785), 20140123. https://doi.org/10.1098/rspb.2014.0123

Bednaršek, N., Harvey, C. J., Kaplan, I. C., Feely, R. A., & Mozina, J. (2016). Pteropods on the edge: Cumulative effects of ocean acidification, warming, and deoxygenation. *Progress in Oceanography*, 145, 1–24. https://doi.org/10.1016/j.pocean.2016.04.002

Bednaršek, N., Klinger, T., Harvey, C. J., Weisberg, S., McCabe, R. M., Feely, R. A., et al. (2017). New ocean, new needs: Application of pteropod shell dissolution as a biological indicator for marine resource management. *Ecological Indicators*, 76, 240–244. https://doi.org/10.1016/j.ecolind.2017.01.025

Caldeira, K., & Wickett, M. E. (2003). Anthropogenic carbon and ocean pH. *Nature*, 425(6956), 365–365. https://doi.org/10.1038/425365a

Cameron, D. R., Lenton, T. M., Ridgwell, A. J., Shepherd, J. G., Marsh, R., & Yool, A. (2005). A factorial analysis of the marine carbon cycle and ocean circulation controls on atmospheric CO_2. *Global Biogeochemical Cycles*, 19, GB4027. https://doi.org/10.1029/2005GB002489

Carter, B. R., Feely, R. A., Williams, N. L., Dickson, A. G., Fong, M. B., & Takeshita, Y. (2018). Updated methods for global locally interpolated estimation of alkalinity, pH, and nitrate. *Limnology and Oceanography: Methods*, 16(2), 119–131.

Carter, B. R., Talley, L. D., & Dickson, A. G. (2014). Mixing and remineralization in waters detrained from the surface into Subantarctic Mode Water and Antarctic Intermediate Water in the southeastern Pacific. *Journal of Geophysical Research, Oceans*, 119(6), 4001–4028. https://doi.org/10.1002/2013JC009355

Clement, D., & Gruber, N. (2018). The eMLR(C*) Method to determine decadal changes in the global ocean storage of anthropogenic CO_2. *Global Biogeochemical Cycles*, 32(4), 654–679. https://doi.org/10.1002/2017GB005819

Couldrey, M. P., Oliver, K. I. C., Yool, A., Halloran, P. R., & Achterberg, E. P. (2019). Drivers of 21st century carbon cycle variability in the North Atlantic Ocean. *Biogeosciences Discussions*, 2019, 1–33.

Deutsch, C., Gruber, N., Key, R. M., Sarmiento, J. L., & Ganachaud, A. (2001). Denitrification and N_2 fixation in the Pacific Ocean. *Global Biogeochemical Cycles*, 15, 483–506.

Deutsch, C., & Weber, T. (2012). Nutrient ratios as a tracer and driver of ocean biogeochemistry. *Annual Review of Marine Science*, 4, 113–141. https://doi.org/10.1146/annurev-marine-120709-142821

Dickson, A. G. (1990). Standard potential of the reaction: AGCL(S) + 1/2H − 2(G) = AG(S) + HCL (AQ) and the standard acidity constant of the ion HSO_4^- in synthetic sea-water from 273.15-K to 318.15-K. *Journal of Chemical Thermodynamics*, 22(2), 113–127.

Duteil, O., Koeve, W., Oschlies, A., Aumont, O., Bianchi, D., Bopp, L., et al. (2012). Preformed and regenerated phosphate in ocean general circulation models: Can right total concentrations be wrong? *Biogeosciences*, *9*(5), 1797–1807. https://doi.org/10.5194/bg-9-1797-2012

Eggleston, S., & Galbraith, E. D. (2018). The devil's in the disequilibrium: Multi-component analysis of dissolved carbon and oxygen changes under a broad range of forcings in a general circulation model. *Biogeosciences*, *15*(12), 3761–3777.

Fabry, V. J., Seibel, B. A., Feely, R. A., & Orr, J. C. (2008). Impacts of ocean acidification on marine fauna and ecosystem processes. *ICES Journal of Marine Science*, *65*(3), 414–432.

Fassbender, A. J., Rodgers, K. B., Palevsky, H. I., & Sabine, C. L. (2018). Seasonal asymmetry in the evolution of surface ocean pCO$_2$ and pH thermodynamic drivers and the influence on sea-air CO$_2$ flux. *Global Biogeochemical Cycles*, *32*(10), 1476–1497. https://doi.org/10.1029/2017GB005855

Feely, R. A., Alin, S., Carter, B., Bednaršek, N., Hales, B., Chan, F., et al. (2016). Chemical and biological impacts of ocean acidification along the west coast of North America. *Estuarine, Coastal and Shelf Science*, *183*(A), 260–270. https://doi.org/10.1016/j.ecss.2016.08.043

Feely, R. A., Doney, S. C., & Cooley, S. R. (2009). Ocean acidification: Present conditions and future changes in a high-CO$_2$ world. *Oceanography*, *22*(4), 36–47.

Feely, R. A., Okazaki, R. R., Cai, W.-J., Bednaršek, N., Alin, S. R., Byrne, R. H., & Fassbender, A. (2018). The combined effects of acidification and hypoxia on pH and aragonite saturation in the coastal waters of the Californian Current Ecosystem and the northern Gulf of Mexico. *Continental Shelf Research*, *152*, 50–60. https://doi.org/10.1016/j.csr.2017.11.002

Feely, R. A., Sabine, C. L., Byrne, R. H., Millero, F. J., Dickson, A. G., Wanninkhof, R., et al. (2012). Decadal changes in the aragonite and calcite saturation state of the Pacific Ocean. *Global Biogeochemical Cycles*, *26*, GB3001. https://doi.org/10.1029/2011GB004157

Feely, R. A., Sabine, C. L., Lee, K., Berelson, W., Kleypas, J., Fabry, V., & Millero, F. J. (2004). Impact of anthropogenic CO$_2$ on the CaCO$_3$ system in the oceans. *Science*, *305*(5682), 362–366. https://doi.org/10.1126/science.1097329

Feely, R. A., Sabine, C. L., Lee, K., Millero, F. J., Lamb, M. F., Greeley, D., et al. (2002). In situ calcium carbonate dissolution in the Pacific Ocean. *Global Biogeochemical Cycles*, *16*(4), 1144. https://doi.org/10.1029/2002GB001866

Franco, A. C., Gruber, N., Frolicher, T. L., & Artman, L. K. (2018). Contrasting impact of future CO$_2$ emission scenarios on the extent of CaCO$_3$ mineral undersaturation in the Humboldt Current System. *Journal of Geophysical Research: Oceans*, *123*(3), 2018–2036. https://doi.org/10.1002/2018JC013857

Frigstad, H., Andersen, T., Hessen, D. O., Naustvoll, L. J., Johnsen, T. M., & Bellerby, R. G. J. (2011). Seasonal variation in marine C:N:P stoichiometry: Can the composition of seston explain stable Redfield ratios? *Biogeosciences*, *8*(10), 2917–2933.

Garcia, H. E., & Gordon, L. I. (1992). Oxygen solubility in seawater: Better fitting equations. *Limnology and Oceanography*, *37*(6), 1307–1312.

Gattuso, J.-P., Magnan, A., Bille, R., Cheung, W. W. L., Howes, E. L., Joos, F., et al. (2015). Contrasting futures for ocean and society from different anthropogenic CO$_2$ emission scenarios. *Science*, *349*(6243), aac4722. https://doi.org/10.1126/science.aac4722

Gebbie, G., & Huybers, P. (2011). How is the ocean filled? *Geophysical Research Letters*, *38*(6), L06604. https://doi.org/10.1029/2011GL046769

Geider, R., & La Roche, J. (2002). Redfield revisited: Variability of C:N:P in marine microalgae and its biochemical basis. *European Journal of Phycology*, *37*(1), 1–17.

Gruber, N., Clement, D., Carter, B. R., Feely, R. A., van Heuven, S., Hoppema, M., et al. (2019). The oceanic sink for anthropogenic CO$_2$ from 1994 to 2007. *Science*, *363*(6432), 1193–1199. https://doi.org/10.1126/science.aau5153

Gruber, N., Sarmiento, J. L., & Stocker, T. F. (1996). An improved method for detecting anthropogenic CO$_2$ in the oceans. *Global Biogeochemical Cycles*, *10*(4), 809–837.

Guinotte, J. M., Buddemeier, R. W., & Kleypas, J. A. (2003). Future coral reef habitat marginality: Temporal and spatial effects of climate change in the Pacific basin. *Coral Reefs*, *22*(4), 551–558.

Hall, T. M., Haine, T. W. N., & Waugh, D. W. (2002). Inferring the concentration of anthropogenic carbon in the ocean from tracers. *Global Biogeochemical Cycles*, *16*(4), 1131. https://doi.org/10.1029/2001GB001835

Hauri, C., Gruber, N., Vogt, M., Doney, S. C., Feely, R. A., Lachkar, Z., et al. (2013). Spatiotemporal variability and long-term trends of ocean acidification in the California Current System. *Biogeosciences*, *10*(1), 193–216.

He, Y.-C., Tjiputra, J., Langehaug, H. R., Jeansson, E., Gao, Y., Schwinger, J., & Olsen, A. (2018). A model-based evaluation of the inverse Gaussian transit-time distribution method for inferring anthropogenic carbon storage in the ocean. *Journal of Geophysical Research, Oceans*, *123*, 1777–1800. https://doi.org/10.1002/2017JC013504

Hurd, C. L., & Cornwall, C. E. (2015). Experimental design in ocean acidification research: Problems and solutions. *ICES Journal of Marine Science*, *73*(3), 572–581.

IPCC (2013). Summary for policymakers. In T. F. Stocker, D. Qin, G.-K. Plattner, M. Tignor, S. K. Allen, J. Boschung, A. Nauels, Y. Xia, V. Bex, & P. M. Midgley (Eds.), *Climate Change 2013: The Physical Science Basis. Contribution of Working Group I to the Fifth Assessment Report of the Intergovernmental Panel on Climate Change*. Cambridge, United Kingdom and New York, NY, USA: Cambridge University Press.

Ito, T., Follows, M. J., & Boyle, E. A. (2004). Is AOU a good measure of respiration in the oceans? *Geophysical Research Letters*, *31*, L17305. https://doi.org/10.1029/2004GL020900

Jiang, L.-Q., Carter, B. R., Feely, R. A., Lauvset, S. K., & Olsen, A. (2019). Surface ocean pH and buffer capacity: Past, present and future. *Scientific Reports*, *9*(1), 18624. https://doi.org/10.1038/s41598-019-55039-4

Jiang, L.-Q., Feely, R. A., Carter, B. R., Greeley, D. J., Gledhill, D. K., & Arzayus, K. M. (2015). Climatological distribution of aragonite saturation state in the global oceans. *Global Biogeochemical Cycles*, *29*(10), 1656–1673. https://doi.org/10.1002/2015GB005198

Kanamori, S., & Ikegami, H. (1982). Calcium-alkalinity relationship in the North Pacific. *Journal of the Oceanographical Society of Japan*, *38*(2), 57–62.

Keeling, R. F., Körtzinger, A., & Gruber, N. (2010). Ocean deoxygenation in a warming world. *Annual Review of Marine Science*, *2*(1), 199–229.

Khatiwala, S., Tanhua, T., Mikaloff Fletcher, S., Gerber, M., Doney, S. C., Graven, H. D., et al. (2013). Global ocean storage of anthropogenic carbon. *Biogeosciences*, *10*(4), 2169–2191. https://doi.org/10.5194/bg-10-2169-2013

Kroeker, K. J., Kordas, R. L., Crim, R., Hendriks, I. E., Ramajo, L., Singh, G. S., et al. (2013). Impacts of ocean acidification on marine organisms: Quantifying sensitivities and interaction with warming. *Global Change Biology*, *19*(6), 1884–1896. https://doi.org/10.1111/gcb.12179

Körtzinger, A., Hedges, J. I., & Quay, P. D. (2001). Redfield ratios revisited: Removing the biasing effect of anthropogenic CO$_2$. *Limnology and Oceanography*, *46*(4), 964–970.

Landschützer, P., Gruber, N., Bakker, D. C. E., Stemmler, I., & Six, K. D. (2018). Strengthening seasonal marine CO_2 variations due to increasing atmospheric CO_2. *Nature Climate Change*, *8*(2), 146–150.

Lauvset, S. K., Gruber, N., Landschützer, P., Olsen, A., & Tjiputra, J. (2015). Trends and drivers in global surface ocean pH over the past 3 decades. *Biogeosciences*, *12*(5), 1285–1298.

Lauvset, S. K., Key, R. M., Olsen, A., van Heuven, S., Velo, A., Lin, X., et al. (2016). A new global interior ocean mapped climatology: The 1° × 1° GLODAP version 2. *Earth System Science Data*, *8*(2), 325–340. https://doi.org/10.5194/essd-8-325-2016

Lenton, A., Metzl, N., Takahashi, T., Kuchinke, M., Matear, R. J., Roy, T., et al. (2012). The observed evolution of oceanic pCO_2 and its drivers over the last two decades. *Global Biogeochemical Cycles*, *26*, GB2021. https://doi.org/10.1029/2011GB004095

Lewis, E., & Wallace, D. W. R. (1998). Program developed for CO_2 system calculations, in *ORNL/CDIAC-105*, edited, Carbon Dioxide Information Analysis Center, Oak Ridge National Laboratory, U.S. Department of Energy, Oak Ridge, Tennessee.

Li, Y.-H., & Peng, T.-H. (2002). Latitudinal change of remineralization ratios in the oceans and its implication for nutrient cycles. *Global Biogeochemical Cycles*, *16*(4), 1130. https://doi.org/10.1029/2001GB001828

Lueker, T. J., Dickson, A. G., & Keeling, C. D. (2000). Ocean $pCO(2)$ calculated from dissolved inorganic carbon, alkalinity, and equations for K-1 and K-2: Validation based on laboratory measurements of CO_2 in gas and seawater at equilibrium. *Marine Chemistry*, *70*(1-3), 105–119.

Martin, J. H., Knauer, G. A., Karl, D. M., & Broenkow, W. W. (1987). VERTEX: Carbon cycling in the northeast Pacific. *Deep Sea Research Part A. Oceanographic Research Papers*, *34*(2), 267–285. https://doi.org/10.1016/0198-0149(87)90086-0

Millero, F. J. (2013). *Chemical Oceanography* (Fourth ed.). Boca Raton, FL: CRC Press Taylor & Francis.

Negrete-García, G., Lovenduski, N. S., Hauri, C., Krumhardt, K. M., & Lauvset, S. K. (2019). Sudden emergence of a shallow aragonite saturation horizon in the Southern Ocean. *Nature Climate Change*, *9*(4), 313–317. https://doi.org/10.1038/s41558-019-0418-8

Olsen, A., Key, R. M., van Heuven, S., Lauvset, S. K., Velo, A., Lin, X., et al. (2016). The Global Ocean Data Analysis Project version 2 (GLODAPv2): An internally consistent data product for the world ocean. *Earth System Science Data*, *8*(2), 297–323. https://doi.org/10.5194/essd-8-297-2016

Olsen, A., Lange, N., Key, R. M., Tanhua, T., Álvarez, M., Becker, S., et al. (2019). GLODAPv2.2019: An update of GLODAPv2. *Earth System Science Data*, *11*(3), 1437–1461. https://doi.org/10.5194/essd-11-1437-2019

Orr, J. C., Epitalon, J.-M., Dickson, A. G., & Gattuso, J.-P. (2018). Routine uncertainty propagation for the marine carbon dioxide system. *Marine Chemistry*, *207*, 84–107. https://doi.org/10.1016/j.marchem.2018.10.006

Osborne, E. B., Thunell, R. C., Gruber, N., Feely, R. A., & Benitez-Nelson, C. R. (2019). Decadal variability in twentieth-century ocean acidification in the California Current Ecosystem. *Nature Geoscience*, *13*(1), 43–49. https://doi.org/10.1038/s41561-019-0499-z

Pardo, P. C., Vázquez-Rodríguez, M., Pérez, F. F., & Rios, A. F. (2011). CO_2 air–sea disequilibrium and preformed alkalinity in the Pacific and Indian Oceans calculated from subsurface layer data. *Journal of Marine Systems*, *84*(3), 67–77.

Park, P. K. (1969). Oceanic CO_2 system: An evaluation of ten methods of investigation. *Limnology and Oceanography*, *14*(2), 179–186.

Redfield, A. C., Ketchum, B. H., & Richards, F. A. (1963). The influence of organisms on the composition of sea water. In M. N. Hill (Ed.), *The Sea* (pp. 26–77). Hoboken, NJ: Wiley-Interscience.

Russell, J. L., & Dickson, A. G. (2003). Variability in oxygen and nutrients in South Pacific Antarctic Intermediate Water. *Global Biogeochemical Cycles*, *17*(2), 1033. https://doi.org/10.1029/2000GB001317

Sabine, C. L., Feely, R. A., Gruber, N., Key, R. M., Lee, K., Bullister, J. L., et al. (2004). The oceanic sink for anthropogenic CO_2. *Science*, *305*(5682), 367–371. https://doi.org/10.1126/science.1097403

Sarmiento, J. L., & Gruber, N. (2006). *Ocean biogeochemical dynamics, XII* (p. 503). Princeton, NJ: Princeton University Press.

Schmittner, A., Gruber, N., Mix, A. C., Key, R. M., Tagliabue, A., & Westberry, T. K. (2013). Biology and air-sea gas exchange controls on the distribution of carbon isotope ratios (delta C-13) in the ocean. *Biogeosciences*, *10*(9), 5793–5816.

Sulpis, O., Boudreau, B. P., Mucci, A., Jenkins, C., Trossman, D. S., Arbic, B. K., & Key, R. M. (2018). Current $CaCO_3$ dissolution at the seafloor caused by anthropogenic CO_2. *Proceedings of the National Academy of Sciences of the United States of America*, *115*(46), 11700–11705. https://doi.org/10.1073/pnas.1804250115

Takahashi, T., Broecker, W. S., & Langer, S. (1985). Redfield Ratio Based on Chemical Data from Isopycnal Surfaces, *Journal of Geophysical Research*, *90*(C4), 6907–6924.

Talley, L. D. (2013). Closure of the global overturning circulation through the Indian, Pacific, and Southern Oceans: Schematics and transports. *Oceanography*, *26*(1), 80–97. https://doi.org/10.5670/oceanog.2013.07

Talley, L. D., Lobanov, V., Ponomarev, V., Salyuk, A., Tishchenko, P., Zhabin, I., & Riser, S. (2003). Deep convection and brine rejection in the Japan Sea. *Geophysical Research Letters*, *30*(4), 1159. https://doi.org/10.1029/2002GL016451

Uppström, L. R. (1974). The boron/chlorinity ratio of deep-sea water from the Pacific Ocean. *Deep Sea Research and Oceanographic Abstracts*, *21*(2), 161–162.

van Heuven, S., Pierrot, D., Lewis, E., & Wallace, D. (2009). MATLAB Program developed for CO_2 system calculations, ORNL/CDIAC-105b, Carbon Dioxide Information Analysis Center, Oak Ridge National Laboratory, US Department of Energy, Oak Ridge, Tennessee.

Vazquez-Rodriguez, M., Touratier, F., Lo Monaco, C., Waugh, D. W., Padin, X. A., Bellerby, R. G. J., et al. (2009). Anthropogenic carbon distributions in the Atlantic Ocean: Data-based estimates from the Arctic to the Antarctic. *Biogeosciences*, *6*(3), 439–451.

Waldbusser, G. G., Hales, B., & Haley, B. A. (2015). Calcium carbonate saturation state: On myths and this or that stories. *ICES Journal of Marine Science*, *73*(3), 563–568.

Waugh, D. W., Hall, T. M., McNeil, B. I., Key, R., & Matear, R. J. (2006). Anthropogenic CO_2 in the oceans estimated using transit time distributions. *Tellus Series B: Chemical and Physical Meteorology*, *58*(5), 376–389.

Wolf-Gladrow, D. A., Zeebe, R. E., Klaas, C., Kortzinger, A., & Dickson, A. G. (2007). Total alkalinity: The explicit conservative expression and its application to biogeochemical processes. *Marine Chemistry*, *106*(1-2), 287–300.

Zeebe, R. E., & Wolf-Gladrow, D. (2001). *CO_2 in seawater, equilibrium, kinetics, isotopes, XIII* (p. 346). Amsterdam, PAYS-BAS: Elsevier.

References From the Supporting Information

Key, R. M., Kozyr, A., Sabine, C. L., Lee, K., Wanninkhof, R., Bullister, J. L., et al. (2004). A global ocean carbon climatology: Results from Global Data Analysis Project (GLODAP). *Global Biogeochemical Cycles*, *18*, GB4031. https://doi.org/10.1029/2004GB002247